Theoretical analysis of the influence of defect parameters on photovoltaic performances of composition graded InGaN solar cells

V. Gorge, A. Migan-Dubois, Zakaria Djebbour, K. Pantzas, Simon Gautier, Tarik Moudakir, Abdallah Ougazzaden, Suresh Sundaram

Theoretical analysis of the influence of defect parameters on photovoltaic performances of composition graded InGaN solar cells

V. Gorge [a], A. Migan-Dubois [a], Z. Djebbour [a,b,*], K. Pantzas [c,d], S. Gautier [d,e], T. Moudakir [d], S. Suresh [d], A. Ougazzaden [c,d]

[a] *LGEP, UMR 8507, CNRS, SUPELEC, UPMC, Université Paris-Sud 11, 11 rue Joliot-Curie, Plateau de Moulon, 91192 Gif-sur-Yvette Cedex, France*
[b] *Department of Physics and Engineering Science, University of Versailles UVSQ, 45 Av. Des Etats Unis, 78035 Versailles, France*
[c] *Georgia Institute of Technology, GT-Lorraine, 2 rue Marconi, 57 070 Metz, France*
[d] *UMI 2958 Georgia Tech, CNRS, 2 rue Marconi, 57 070 Metz, France*
[e] *LMOPS, UMR 7132, CNRS, University of Metz, Supélec, 2 rue E. Belin, 57 070 Metz, France*

In this paper, we have used simulations to evaluate the impact of the distribution of electrically active defects on the photovoltaic performances of InGaN-based solar cell. The simulations were carried out using Silvaco's ATLAS software. We have modeled a P-GaN/Grad-InGaN/i-$In_{0.53}Ga_{0.47}N$/Grad-InGaN/N-ZnO where Grad-InGaN corresponds to an InGaN layer with a graded composition. This layer is inserted to eliminate the band discontinuities at the interface between InGaN and the GaN and ZnO layers. The defects were modeled through the introduction of band tails and a Gaussian distribution of defects in i-InGaN material. We have evaluated the influence of band tail widths as well as the parameters of the Gaussian distribution (i.e. defect density, mean position and standard deviation) on the short-circuit current, the open-circuit voltage and the fill-factor (efficiency) of the solar cell. These results have allowed us to identify key structural parameters useful for the optimization of InGaN solar cells, as well as to give realistic estimates of the performances of such cells.

1. Introduction

For the last 10 years, InGaN alloys have been intensively studied for terrestrial solar cell applications [1]. The main attractive characteristic of this alloy is its large tunable direct bandgap from infrared (0.78 eV) with high indium concentration to ultraviolet (3.51 eV) for high gallium percentage [2,3]. Thus InGaN multi-junction devices are predicted to be able to achieve an efficiency of >70% [4]. This multi-junction solar cell can also be used in conjunction with concentrated light. The current world record in efficiency is 43.5%, for a GaInP–GaInAs–Ge triple-junction tandem solar cell in a concentrator system [5]. However, this efficiency is approaching its theoretical limit defined by its band gaps. Hence, it is quite interesting to study such InGaN solar cells, possessing a larger band gap.

However, experimental InGaN-based solar cell performance [6,7] stays much lower than predicted [8]. One of the explanations is the InGaN high defect density, which is due to lattice mismatch with the substrate, indium incorporation in GaN lattice, or impurities. Reported papers generally studied only defect density [9], but it is also interesting to investigate the other defect parameters such as activation energy or standard deviation. In this paper, we report on the impact of different defect characteristics present in the InGaN material on solar cell efficiency.

2. Model description

The simulations were carried out using Silvaco's ATLAS software. It is a physically-based two and three-dimensional device simulator. It predicts the electrical behavior of specified semiconductor structures and provides insight into the internal physical mechanisms associated with device operation. In our investigated model, all the physical parameters have been chosen varying only in the direction normal to the heterointerfaces, which suppose the uniformity of the layers in other orthogonal directions.

The structure of the cell is represented schematically in Fig. 1. The corresponding finite element mesh is shown in Fig. 2. A non-uniform mesh was used to obtain good accuracy in reasonable calculation times. The grid is denser at the interface, where we expect the most variations to occur. The cell is based on a p–i–n junction. The absorption occurs within the intrinsic layer composed by $In_{0.53}Ga_{0.47}N$. The bandgap of this alloy is equal to

* Corresponding author at: LGEP, UMR 8507, CNRS, SUPELEC, UPMC, Université Paris-Sud 11, 11 rue Joliot-Curie, Plateau de Moulon, 91192 Gif-sur-Yvette Cedex, France. Tel.: +33 1 69 85 16 42; fax: +33 1 69 41 83 18.
E-mail address: zakaria.djebbour@uvsq.fr (Z. Djebbour).

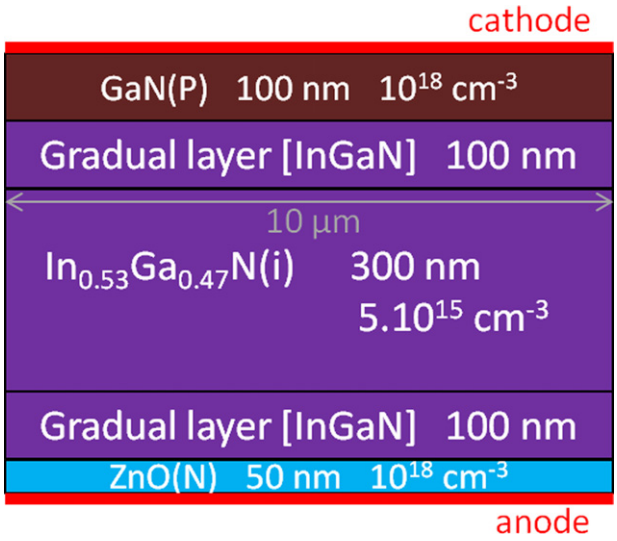

Fig. 1. Structure of the p–i–n junction used for simulations with gradual bandgap layers.

1.7 eV. According to previous simulations, band alignment between $In_{0.53}Ga_{0.47}N$ conduction band and Si valence band occurs, leading to a low resistance ohmic contact [10]. Simulations have reported InGaN/Si tandem solar cell efficiency up to 31% [11]. In our simulation, the P-doped layer is composed by GaN. Contrarily, ZnO forms the N-doped layer, which is also the substrate. The advantage of ZnO over GaN is the lattice mismatch reduction with $In_{0.53}Ga_{0.47}N$. In addition, ZnO has very close properties with GaN such as bandgap, intrinsic N-type doping, crystalline structure, and electron mobility, leading to similar electrical properties with lower defect density. Gradual bandgap layers have been introduced between the doped and the absorber layers in order to limit the presence of barriers at the interfaces. Indeed, we previously found that the efficiency of a simple p–i–n junction as described above drops dramatically when the barrier is higher than 0.9 eV, corresponding to only 10% of indium in the InGaN alloy [18]. The bandgap of the material in these layers linearly varies from the value of GaN from the one to InGaN. At the gradual bandgap layer and ZnO interface, the conduction bands have been aligned in order to not

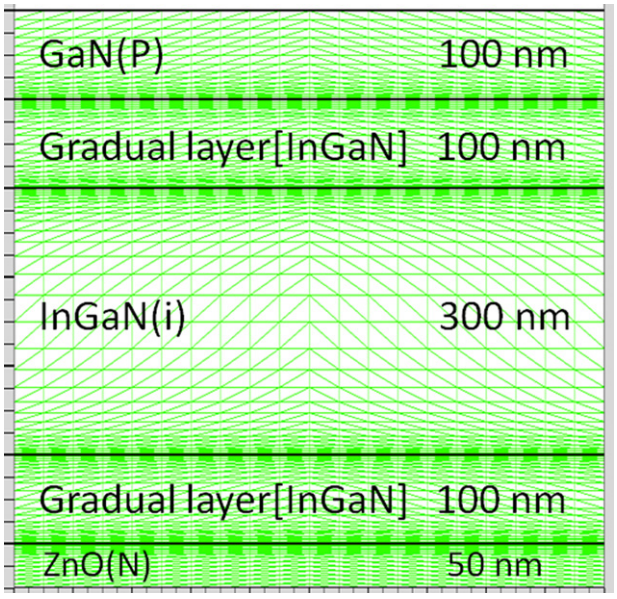

Fig. 2. The mesh of the structure.

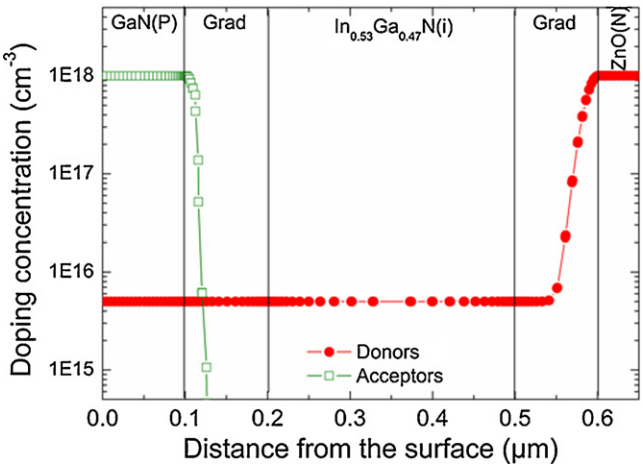

Fig. 3. Doping profile through the device.

create any barrier for electron. This leads to a remaining low indium percentage in the InGaN alloy near the ZnO layer equals to 1%.

The thicknesses of the absorber and graded layers have been optimized separately. Simulations were done for absorber thickness varying from 10 nm to 500 nm and we have found that the optimal thickness was 300 nm. As well, previous simulations have also shown that the efficiency significantly decreases when graded layers are larger than 100 nm. We have thus fixed the thickness of the gradual bandgap layers at 100 nm. The thickness of the GaN P-type layer has been fixed at 100 nm because it is a currently experimental used thickness for this layer [6,12]. Finally, the thickness of the ZnO N-type layer has been fixed to 50 nm in order to optimize the calculation time. Indeed, the N-type layer is generally larger but its thickness does not influence solar cell performances since the electron mobility is high (around 300 cm^2 V^{-1} s^{-1} for electrons in ZnO at 300 K). So, in order to reduce the calculation time, we have used a thin N-type layer.

The doping concentration in each material is also shown in Fig. 1. The P- and N-layers doping concentration has been fixed to average experimental values, 10^{18} cm^{-3} [13,14]. To model the intrinsic electrical N-type behavior of InGaN, a low N-type doping of 5×10^{15} cm^{-3} has been introduced in the absorber and the graded layers [15]. To model a realistic junction, diffusion of dopants has been taken into account using Gaussian profiles at the interfaces, as shown in Fig. 3.

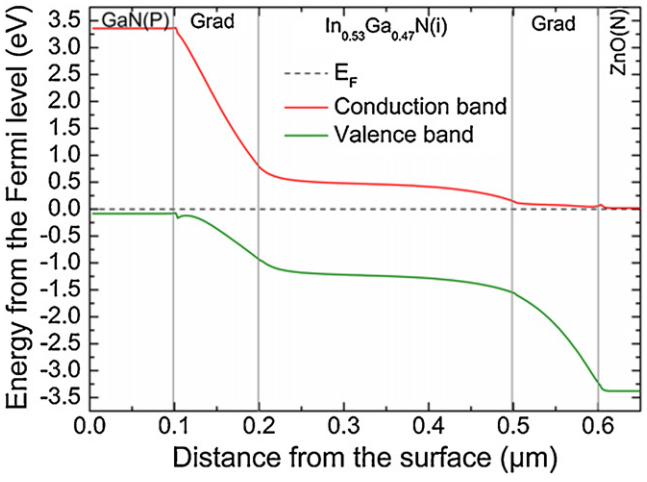

Fig. 4. Band diagram trough the device.

Table 1
Material parameters used in the model for the InGaN, the GaN and the ZnO materials.

	GaN	$In_{0.53}Ga_{0.47}N$	ZnO
Bandgap at 300 K (eV)	3.44	3.06	3.4
Electron affinity (eV)	4.20	4.573	4.35
SRH lifetime (s) for electrons	1.70×10^{-9}	1.70×10^{-9}	
SRH lifetime (s) for holes	0.65×10^{-9}	0.65×10^{-9}	

The band diagram is presented in Fig. 4. The variation of the bandgap in the gradual bandgap layers is visible. No barrier is present at the interfaces, which ensures good carrier collection. Polarization effects have been taken into account in the model.

The following model was used for the *n* and *p* electrodes: ohmic, transparent, with no additional series resistance. The electrodes cover the entire surface for the cathode and the bottom of the device for the anode.

The parameters used to define materials are given in Table 1. They are composed by the *n* and *k* parameters between 250 and 1300 nm for absorption, the bandgap, and the electron affinity of the materials. Shockley–Read–Hall recombination parameters are also introduced. They model non-radiative recombinations occurring in point defects, which depend on the density of states present within the bandgap, the defect energy level, and electron and hole lifetimes. The optical and Auger recombinations have been found to be negligible. In addition, valence band splitting in three branches present in wurtzite materials has been taken into account using the model proposed by Chuang and Chang [16].

Doping concentration dependent carrier mobilities were obtained for GaN and InGaN using the Caughey–Thomas model. This model is defined by the following equation [1–8,17]:

$$\mu_i(N) = \mu_{\min,\,i} + \frac{\mu_{\max,\,i} - \mu_{\min,\,i}}{1 + (N/N_{g,\,i})}$$

where *i* represents either electrons (e) or holes (h), *N* is the doping concentration and $\mu_{\min}$, $\mu_{\max}$, γ and N_g are parameters specific to a given semiconductor. The values used for these parameters are given in Table 2. Carrier mobilities in ZnO were fixed to 2000 for electrons and 30 $cm^2\,V^{-1}\,s^{-1}$ for holes [19].

The modeling of the high defect density intrinsically present in nitrides has been taken a leaf out of amorphous silicon. It is composed by two band tails and one donor localized energy level modeled by a Gaussian distribution, introduced in InGaN. This is shown in Fig. 5. In the proposed model, band tails are described by their conduction and valence band edge intercepts densities (N_c and N_v), and by their characteristic decay energy ($E_{charact}$), a stands for acceptors and d for donnors:

$$g_{ta}(E) = N_c \times \exp\left(\frac{E_v - E}{E_{charact}}\right)$$

$$g_{td}(E) = N_v \times \exp\left(\frac{E - E_c}{E_{charact}}\right)$$

Table 2
Parameters used to calculate the carrier mobility with the Caughey–Thomas model. The parameters for InGaN were linearly interpolated from the end-point values [15,16].

	GaN	$In_{0.53}Ga_{0.47}N$	InN
$\mu_{min,e}$ ($cm^2\,V^{-1}\,s^{-1}$)	55	42	30
$\mu_{max,e}$ ($cm^2\,V^{-1}\,s^{-1}$)	1000	1053	1100
$N_{g,e}$ (cm^{-3})	2×10^{17}	10^{18}	8×10^{18}
γ_e	1	1	1
$\mu_{min,h}$ ($cm^2\,V^{-1}\,s^{-1}$)	3	3	3
$\mu_{max,h}$ ($cm^2\,V^{-1}\,s^{-1}$)	170	260	340
$N_{g,h}$ (cm^{-3})	3×10^{17}	3×10^{17}	3×10^{17}
γ_h	2	2	2

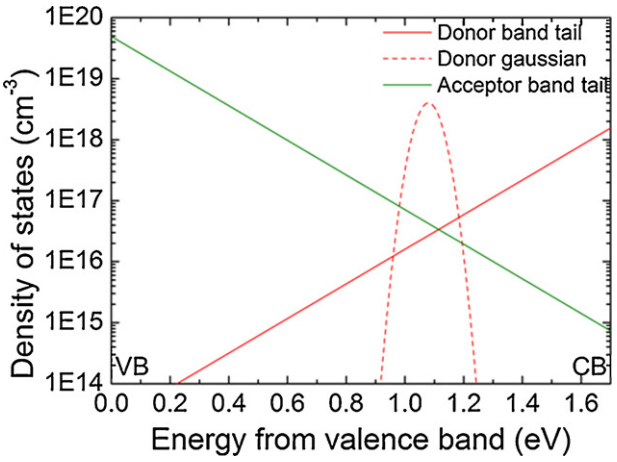

Fig. 5. Schematic of the band tails and the localized energy level in InGaN bandgap.

(i) a characteristic energy ($E_{charact}$) that describes the penetration depth in the bandgap, fixed at 100 meV [20]. The valence and the conduction band tails are supposed to be symmetric;
(ii) valence and conduction densities of states which have been taken equal to their theoretical values at 300 K, $N_v = 1.55 \times 10^{18}\,cm^{-3}\,eV^{-1}$ and $N_c = 4.93 \times 10^{19}\,cm^{-3}\,eV^{-1}$, respectively [21,22];
(iii) a capture cross-section, equal to $10^{-14}\,cm^{-2}$ for both electrons and holes.

The band tails can be physically linked to shallow defects such as nitrogen or gallium vacancies [23]. They can also be strain-induced.

The Gaussian-distributed localized energy level has been modeled by:

(i) a mean position in the InGaN bandgap fixed at 620 meV below the conduction band edge;
(ii) a density equals to $5 \times 10^{17}\,cm^{-3}\,eV^{-1}$;
(iii) a full width at half maximum (FWHM) which was defined at 50 meV;
(iv) a capture cross-section equal to $10^{-14}\,cm^{-2}$ for both electrons and $10^{-16}\,cm^{-2}$ for holes.

This localized defect at 620 meV below the $In_{0.53}Ga_{0.47}N$ conduction band can be linked to donor-type impurities such as carbon or oxygen [23]. The parameters of the band tails and the localized energy level are summarized in Table 3.

Reflections at the surface of the device and between the different layers have also been integrated into the model. The structure was illuminated by a reference AM1.5 solar spectrum to calculate the device performances: We have noted (i) the short-circuit courant density $|J_{sc}|$, i.e. current flowing through the cell when it is short-circuited, (ii) the open-circuit voltage, V_{oc}, (iii) the fill factor

Table 3
Parameters of the defects in InGaN material, band tails and the localized energy level.

	Band tails	Localized energy level
Density ($cm^{-3}\,eV^{-1}$)	$N_v = 1.55 \times 10^{18}$ $N_c = 4.93 \times 10^{19}$	5×10^{17}
Mean position (meV)		620 below CBE
Width (meV)	$E_{charact} = 100$	FWHM = 50
Cross section (cm^{-2})	10^{-14}	10^{-14}

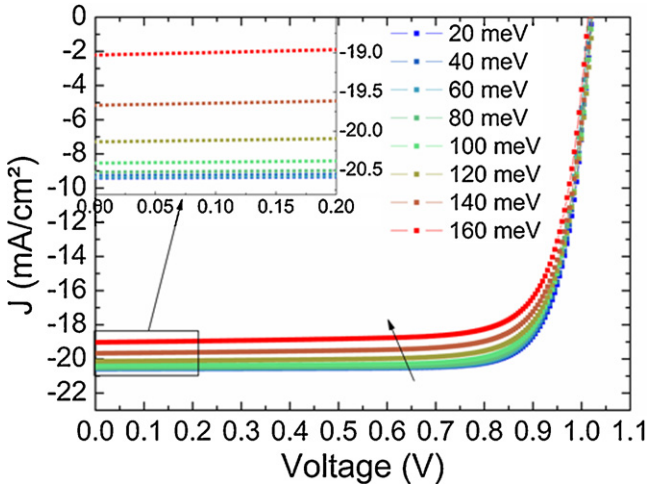

Fig. 6. $I(V)$ characteristic of the solar cell as a function of the band tail characteristic energy. The inset shows the zone between 0 and 0.2 V.

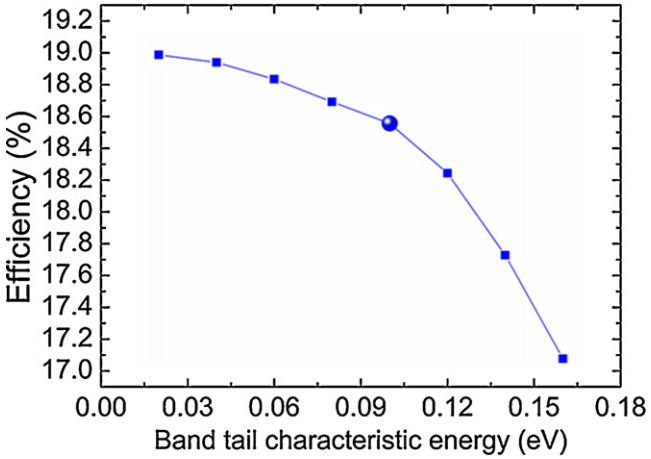

Fig. 7. Efficiency of the device as a function of the band tail characteristic energy. The big dot represents the efficiency of the starting model.

(efficiency), FF, which indicates the degree of ideality of the characteristic and (iv) the conversion efficiency, η. Those parameters are defined by the equations:

$$\eta = \frac{P_m}{E.S}$$

$$FF = \frac{P_m}{J_{sc}.V_{oc}.S}$$

where E is the illumination ($1000\,W\,m^{-2}$), S is the illuminated surface and P_m is the maximum output power of the photovoltaic cell.

3. Results and discussion

The above described InGaN-based solar cell model gives an efficiency of 18.5%. From this model, the band tail characteristic energy, and the density, the FWHM and the energy level of the localized deep defect have been investigated. In each simulation, only one of these parameters was varied, while the others were kept constant to their above defined value. We have studied the influence of these defect parameters on the conversion efficiency of the proposed cell.

3.1. Characteristic energy of the band tail

The characteristic energy of the band tail corresponds to its penetration depth within the material bandgap. It has been varied symmetrically between 20 meV and 160 meV for the valence and the conduction bands. In a previous study, we evaluated this parameter experimentally and found that it was around 100 meV in $In_{0.2}Ga_{0.8}N$ material [20]. The current–voltage curve of the solar cell as a function of the band tail characteristic energy is shown in Fig. 6. The open-circuit voltage, V_{oc}, does not vary with this parameter. On the contrary, the short-circuit current density, $|J_{sc}|$, decreases when the band-tail width increases. This phenomenon can be explained by an increase of the SRH recombination rate leading to a reduction of the device efficiency, as shown in Fig. 7. Nevertheless, the impact of characteristic energy of band tails on efficiency is shown to be relatively small.

3.2. Density of states of the localized energy level

The second studied parameter is the density of states of the localized energy level into the InGaN material which has been varied from $5 \times 10^{14}\,cm^{-3}\,eV^{-1}$ to $5 \times 10^{18}\,cm^{-3}\,eV^{-1}$. The obtained $I(V)$ curves are presented in Fig. 8. The $I(V)$ characteristics, such as V_{oc} or $|J_{sc}|$, do not change as long as the defect DOS stays below $5 \times 10^{17}\,cm^{-3}\,eV^{-1}$. From $10^{18}\,cm^{-3}\,eV^{-1}$, the fill factor (efficiency) strongly decreases with a "S" shape suggesting the presence of a barrier. Then, the $|J_{sc}|$ decreases when the defect DOS is higher than $2 \times 10^{18}\,cm^{-3}\,eV^{-1}$. This result indicates that the defects act as dopants, modifying the doping profile and reducing the space charge zone of the junction.

We can interpret this result by using the equivalent circuit (1 diode) of the solar cell. The electric model is often composed of (i) a diode, representing the behavior of the cell in the dark, (ii) a series resistance, representing the resistive losses of the material and (iii) a shunt resistance modeling parasitic currents which cross the cell. When the defect DOS increases, two cases must be considered:

(i) If defects are found in the space-charge zone, the increase of the defects DOS can create conduction channels and leakage currents associated. This will affect the shunt resistance.
(ii) If defects are found out of the space charge zone, the increase of the defect DOS will increase the non-radiative recombination rate, thus increasing the series resistance.

The solar cell efficiency as a function of the defect density of states is shown in Fig. 9. The efficiency is constant with the defect DOS until $10^{18}\,cm^{-3}\,eV^{-1}$. Then, it drops dramatically. Therefore, the defect DOS has a low influence on conversion efficiency as long as it stays below the threshold of $10^{18}\,cm^{-3}\,eV^{-1}$ in our simulation.

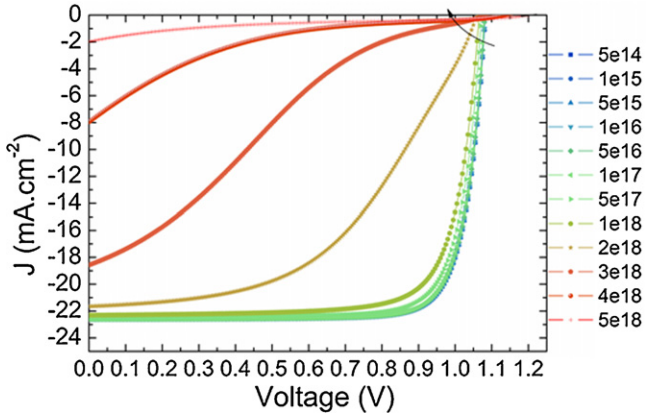

Fig. 8. $I(V)$ characteristics of the device as a function of the density of states.

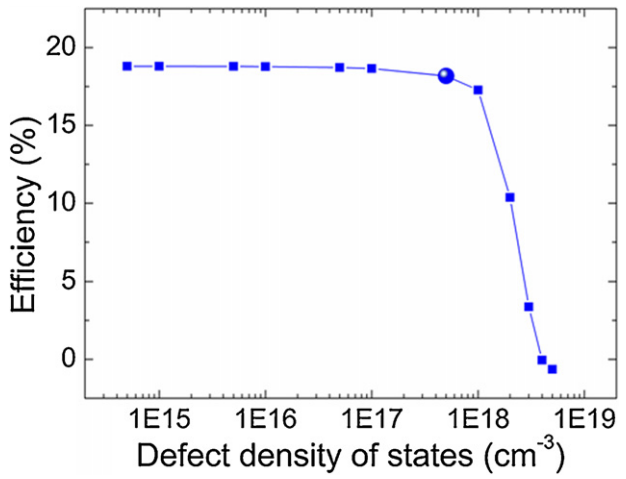

Fig. 9. Efficiency of the solar cell as a function of the defect density of states. The big dot represents the efficiency of the starting model.

3.3. FWHM of the localized energy level

The next parameter is the width of the localized energy level defined by the FWHM. This parameter can be linked to the defect dispersion, the different defect environments; or can model several localized energy levels into the bandgap for the largest widths. The $I(V)$ characteristics of the solar cell is presented in Fig. 10 for deep defect width varying between 10 meV and 800 meV. With the increasing of the FWHM, the $|J_{sc}|$ decreases because of recombination augmentation. The defect acts as a recombination center increasing the SRH rate. The V_{oc}, first, decreases when the FHWM is below 200 meV, and then, increases. In the first part, the defect is located above the Fermi level. Band-to-defect transitions are then allowed reducing the effective material bandgap, and with it the V_{oc}. In the second part, the defect is below the Fermi level, as shown in Fig. 11. The defect energy level is filled by electrons acting as donor. These additional donors increase the N-type character of InGaN, reducing the space charge zone width. This leads to an increase of the electric field in the junction. This phenomenon explains the V_{oc} increase when the FWHM is higher than 200 meV. The solar cell efficiency is presented in Fig. 12. It decreases from 19.5% down to 13.5% with the defect width increase inducing a significant impact of this defect parameter on solar cell performances. Thus, it is theoretically preferable to have as few as possible defect types with short width.

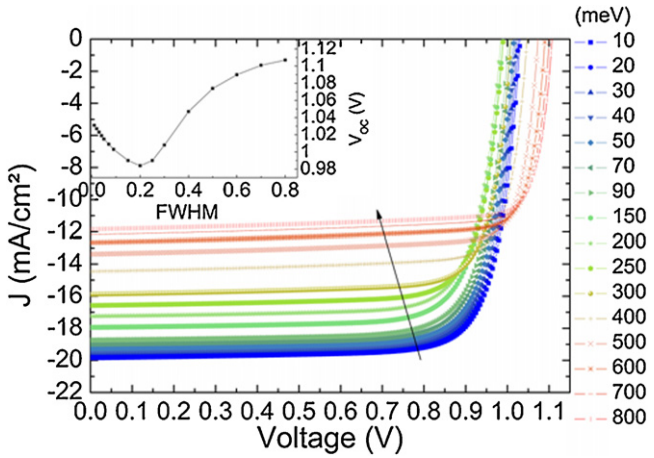

Fig. 10. $I(V)$ characteristics of the device as a function of the localized defect FWHM. The inset shows the V_{oc} as a function of the FWHM.

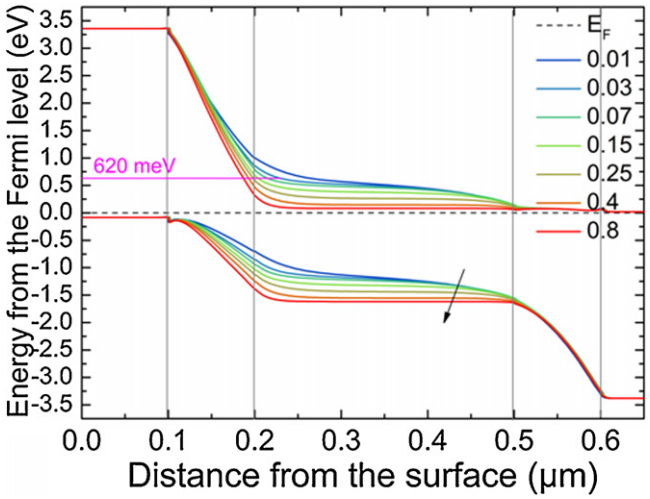

Fig. 11. Band diagram through the structure as a function of the localized defect FWHM.

3.4. Mean position of the localized energy level

The last studied defect parameter is its mean position within the InGaN bandgap. It has been varied between 0.05 eV and 1.55 eV below the conduction band. The obtained $I(V)$ curves are presented in Fig. 13. The insets show the V_{oc} and $|J_{sc}|$ parameters as a function of the mean position of the defect. As the defect is shifted down to the valence band, the $|J_{sc}|$ decreases, with a stable zone between 0.62 eV and 1.2 eV. The V_{oc} first decreases, before a stable zone, and then slightly increases when the defect is located below 1.2 eV from the conduction band. Three zones can then be identified. The first one is near the conduction band, when the defect is located between 0.05 eV and 0.4 eV. In this zone, band-to-defect transitions can occur, leading to a reduction of the effective material bandgap and a V_{oc} decrease. In the same time, the defect starts passing below the Fermi level in the InGaN material limiting recombinations and thus increasing $|J_{sc}|$.

In the second zone, between 0.4 eV and 1.2 eV from the conduction band, V_{oc} and $|J_{sc}|$ are stable. The defect is completely below the Fermi level. It is not correlated with the conduction or the valence bands. The defect acts as a simple recombination center.

Finally, in the third zone, when the defect mean position is below 1.2 eV from the conduction band, near the valence band, V_{oc} and

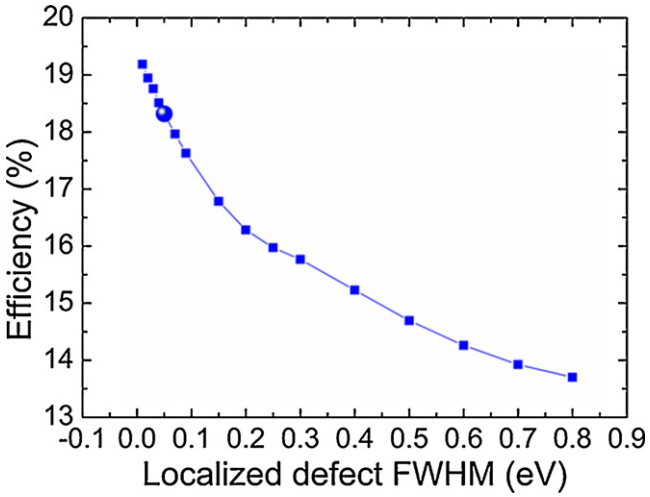

Fig. 12. Efficiency of the solar cell as a function of the localized defect FWHM. The big dot represents the efficiency of the starting model.

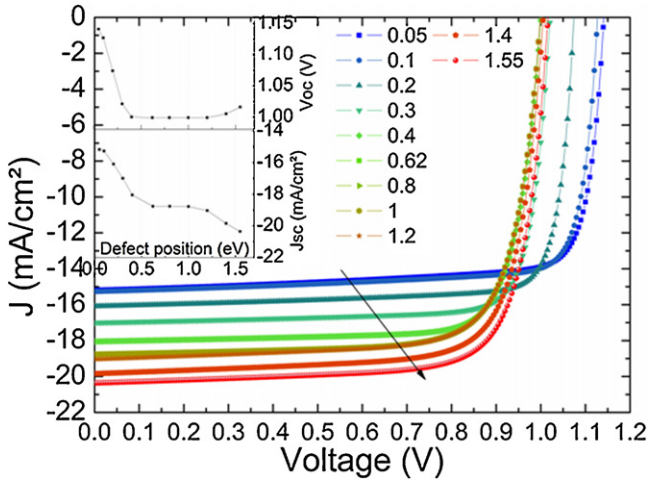

Fig. 13. $I(V)$ characteristics of the device for defect mean positions between 0.05 and 1.55 eV below the conduction band. The insets show the V_{oc} and the $|J_{sc}|$ as a function of the defect mean position.

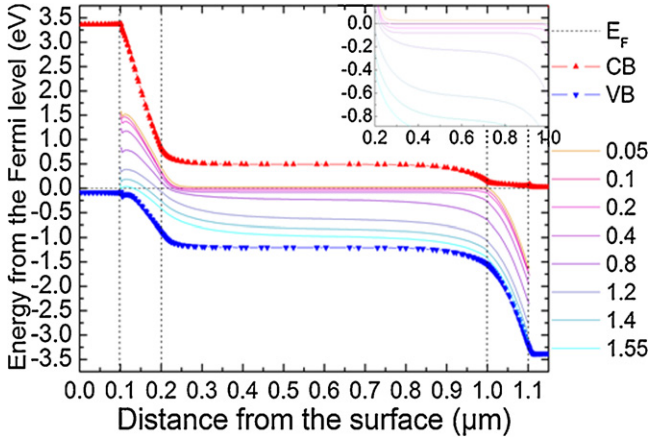

Fig. 14. Band diagram through the structure for defect mean position between 0.05 and 1.55 eV below the conduction band. The defect energy levels are shown by the full lines.

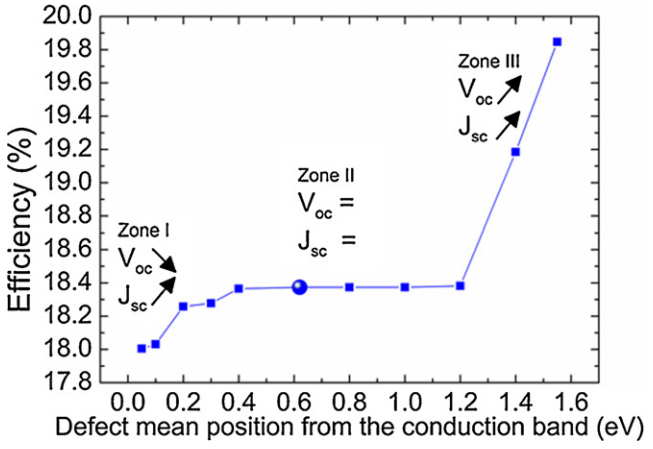

Fig. 15. Efficiency of the solar cell as a function of the defect mean position. Three zones can be identified on this curve. The first one is near the conduction band when V_{oc} decreases and $|J_{sc}|$ increases, the second one is for medium mean positions where V_{oc} and $|J_{sc}|$ are stable, and the third zone is near the valence band where V_{oc} and $|J_{sc}|$ increase. The big dot represents the efficiency of the starting model.

$|J_{sc}|$ increase. In Fig. 14 showing the band diagram through the structure, we see that the defect energy level is pushed below the Fermi level in the gradual bandgap layer, in the junction region. Recombinations are thus reduced leading to a $|J_{sc}|$ increase. With the recombination reduction in the junction area, the V_{oc} slightly increases.

The efficiency of the solar cell as a function of the defect mean position is presented in Fig. 15. The three described zones are also visible in this curve. From this result, it seems better to have defects localized below the Fermi level in order to limit SRH recombinations. Moreover, the absence of additional recombination centers in the junction area improves device performances. Nevertheless, the efficiency increases only from 18% to 19.9% implying that the mean position of the defect has a limited impact on solar cell efficiency.

4. Conclusion

A high efficiency InGaN-based solar cell has been modeled containing gradual bandgap layers, polarization effects and high defect density in InGaN. We reported on a solar cell simulation analysis taking into account a defect model. We have analyzed the characteristic energy of the band tails, and the density, the width and the mean position of a deep localized energy level in the InGaN bandgap. We have found that the defect mean position have a limited impact on the device performances. The band tail width has a medium effect, whereas localized defect width has a significant impact on efficiency. Finally, the impact of localized energy level density of state is negligible as long as it stays strictly lower than 10^{18} cm^{-3} eV^{-1} in our simulation. In general, deep defect parameters seem to have a stronger impact on efficiency than band tail parameter.

Subsequently, it would be interesting to study the following points: (i) the influence of the temperature and the light flux concentration on defects; (ii) the polarization effects which are important in nitride structures; (iii) realistic metal contacts instead of non ideal ohmic contacts; (iv) different electrode configurations (spacing, thickness, etc.).

References

[1] S. Nakamura, M. Senoh, T. Mukai, Applied Physics Letters 62 (1993) 2390.
[2] J. Wu, W. Walukiewicz, K.M. Yu, J.W. Auger III, E.E. Haller, H. Lu, W.J. Schaff, Y. Saito, Y. Nanishi, Applied Physics Letters 80 (2002) 3967.
[3] H.P. Maruska, J.J. Tietjen, Applied Physics Letters 15 (1969) 327.
[4] A. Yamamoto, Md.R. Islam, T.-T. Kang, A. Hashimoto, Physica Status Solidi 7 (2010) 1309.
[5] M.A. Green, K. Emery, Y. Hishikawa, W. Warta, E. Dunlop, Progress in Photovoltaics: Research and Applications 20 (2012) 12.
[6] O. Jani, I. Ferguson, C. Honsberg, S. Kurtz, Applied Physics Letters 91 (2007) 132117.
[7] C.J. Neufeld, N.G. Toledo, S.C. Cruz, M. Iza, S.P. DenBaars, U.K. Mishra, Applied Physics Letters 93 (2008) 143502.
[8] S.P. Bremner, M.Y. Levy, C.B. Honsberg, Progress in Photovoltaics: Research and Applications 16 (2008) 225.
[9] S.-W. Feng, C.-M. Lai, C.-H. Chen, W.-C. Sun, L.-W. Tu, Journal of Applied Physics 108 (2010) 093118.
[10] S.R. Kurtz, P. Faine, J.M. Olson, Journal of Applied Physics 68 (1990) 1890.
[11] L. Hsu, W. Walukiewicz, Journal of Applied Physics 104 (2008) 024507.
[12] J.R. Lang, C.J. Neufeld, C.A. Hurni, S.C. Cruz, E. Matioli, U.K. Mishra, J.S. Speck, Applied Physics Letters 98 (2011) 131115.
[13] X. Wang, S.-B. Che, Y. Ishitani, A. Yoshikawa, Applied Physics Letters 92 (2008) 132108.
[14] N. Koide, H. Kato, M. Sassa, S. Yamasaki, K. Manabe, M. Hashimoto, H. Amano, K. Hiramatsu, I. Akasaki, Journal of Crystal Growth 115 (1991) 639.
[15] E. Gür, Z. Zhang, S. Krishnamoorthy, S. Rajan, A. Ringel, Applied Physics Letters 99 (2011) 092109.
[16] S.L. Chuang, C.S. Chang, Physical Review B 54 (1996) 2491.
[17] Z.Q. Li, M. Lestradet, Y.G. Xiao, S. Li, Physica Status Solidi A 208 (2011) 928.
[18] G.F. Brown, J.W. AgerIII, W. Walukiewicz, J. Wu, Solar Energy Materials and Solar Cells 94 (2010) 478–483.

[19] D.C. Look, D.C. Reynolds, J.R. Sizelove, R.L. Jones, C.W. Litton, G. Cantwell, W.C. Harsch, Solid State Communications 105 (1998) 399.
[20] V. Gorge, Z. Djebbour, A. Migan-Dubois, C. Pareige, C. Longeaud, K. Pantzas, T. Moudakir, S. Gautier, G. Orsal, P.L. Voss, A. Ougazzaden, Applied Physics Letters 99 (2011) 062113.
[21] Ioffe Physico-Techical Intitue. GaN–gallium nitride. New Semiconductor Materials. Charateristics and Properties. http://www.ioffe.ru/SVA/NSM/Semicond/GaN/index.html (online) (cited 30.05.12).
[22] Ioffe Physico-Techical Intitue. InN–Indium nitride. New Semiconductor Materials. Charateristics and Properties. http://www.ioffe.ru/SVA/NSM/Semicond/InN/index.html (online) (cited 30.05.12).
[23] I. Gorczyca, A. Svane, N.E. Christensen, Physical Review B 60 (1999) 8147.